

## In-Process Condition Monitoring in Laser Powder Bed Fusion (LPBF)

Mohammad Montazeri\*, Prahalada Rao\*

\* Mechanical and Materials Engineering Department, University of Nebraska-Lincoln,  
Lincoln, NE 68588

The goal of this work is to monitor the laser powder bed fusion (LPBF) process using an array of heterogeneous sensors. This goal is termed as build status monitoring. The overarching aim is to usher a *qualify-as-you-build* quality assurance paradigm in LPBF whereby incipient build defects are detected through analysis of data acquired from in-process sensors. This will allow opportune preventive action to avert propagation of build defects across multiple layers. In pursuit of this goal, a commercial LPBF machine at the National Institute of Standards and Technology (NIST) was integrated with three types of sensors, namely, a photodetector, high-speed video camera, and SWIR thermal camera with the following objective: to develop and apply a spectral graph theoretic approach to monitor the LPBF build status from the data acquired by the three sensors. This objective will lead to early identification of incipient defects that afflict LPBF despite extensive process automation. The proposed approach is illustrated with experimental sensor data acquired during LPBF of a part having a steep overhang feature of  $\sim 40.5^\circ$ . Parts with such steep overhang features may exacerbate deleterious consequences such as poor surface finish, porosity, and distortion. Hence, close monitoring of the signal patterns during scanning of overhang areas is consequential for early detection of build defects. The proposed approach detected differences between overhang and non-overhang build status for different sensors with the statistical fidelity (F-score) of 95% from thermal camera signatures to 79% with the photodetector. In comparison, conventional signal analysis techniques - e.g., neural networks, support vector machines, linear discriminant analysis, etc., are evaluated with F-score in the range of 40% to 60%. As part of our forthcoming work, this study will be further expanded to include more build defects, e.g., due to material contamination.

Key Words: Laser Powder Bed Fusion (LPBF), Heterogeneous Sensing, In-situ Monitoring, Meltpool Thermal Imaging, High-Speed Imaging, Photodetection, Spectral Graph Theory, Manifold Learning, Laplacian Eigenvectors.

Corresponding author: P. Rao, email:rao@unl.edu

## 1 Introduction

### 1.1 Objective

The goal of this work is to monitor the laser powder bed fusion (LPBF) process using an array of heterogeneous sensors [1]. This goal is termed as build status monitoring. In pursuit of this goal, a commercial LPBF machine (EOS M270) at the National Institute of Standards and Technology (NIST) was integrated with three sensors, namely, a photodetector (spectral response 300 nm to 1200 nm), high-speed video camera (4000 frames/s), and SWIR thermal camera (1350 nm to 1600

nm, calibrated for measuring temperature in the range 500 °C and 1025 °C) with the following objective.

*Objective:* Develop and apply a spectral graph theoretic approach to monitor the build status in LPBF from the data gathered by the three aforementioned sensors. The intent is to detect the onset of deleterious phenomena, such as thermal-induced distortion [2-5]. These phenomena are precursors to part defects, e.g., geometric inaccuracies [5]. In the worst case, these may ultimately result in build failures. The proposed approach is extensible to other AM processes.

This objective will answer the following open research question in the context of in-situ sensing and monitoring in LPBF.

- What sensor signatures (e.g., meltpool shape, spatter pattern) are symptomatic of the build status; and what new analytical approaches are required to extract these signatures from a heterogeneous sensor suite?

## 1.2 Scientific Rationale and Hypotheses

The following two hypotheses corresponding to the objective will be tested in this work.

*Hypothesis 1:* The scientific rationale is that each type of build defect in LPBF is connected with specific process phenomena. The onset of these phenomena manifests in statistically distinctive sensor signatures [6-8]. Hence, by closely tracking the signatures from in-process sensor data the build status in LPBF can be discriminated. Following this reasoning, we posit that given a signal  $\mathcal{X}$ , e.g., photodetector signal, thermal and high-speed video images, converting  $\mathcal{X}$  into a weighted planar network graph  $G(V, E, W)$  with  $V$  vertices, edges  $E$ , and weights  $W$  captures the process phenomena in a lower dimensional manifold.

The central premise is that despite the transformation of the data into a lower dimensional graph space, a large part of the information in the signal is retained, as shown by Belkin and Niyogi [9-11]; Sandryhaila *et al.* [12], Hammond *et al.* [13]; and Shuman *et al.* [14, 15].

We specifically test the hypothesis in Sec. 2 that by representing the sensor data as an weighted and undirected graph  $G(V, E, W)$ , and subsequently using the Eigenvectors ( $v$ ) and Eigenvalues ( $\lambda$ ) of the graph Laplacian as derived sensor signatures, leads to higher classification fidelity in terms of the F-score — which is an aggregate measure of the Type I and Type II statistical error — compared to popular parametric approaches, such as neural networks and support vector machines which rely on statistical features from the sensor data [16].

*Hypothesis 2:* Using the proposed graph Laplacian approach, the classification fidelity with the photodetector is within 20% (F-score) of that obtained through the high-fidelity thermal and video cameras. We test this hypothesis in Sec. 2.3 by comparing the F-score for each of the three sensors in discriminating between the overhang and non-overhang build conditions.

*Remark – Why Monitoring Overhang Versus Non-Overhang Build Status is a Practically Important Problem.*

Overhang features typically require support structures, and are in contact with more metal powder material from below compared to solid, non-overhang features. Insufficient or poorly designed support structures is one of the reasons for build failures [4]. Printing of overhang features is a challenging proposition due to the following reasons [3].

First, referring to Figure 1 (left), as the thermal conductivity of the powder is roughly one third of a solid part, heat tends to accumulate within the overhang area, i.e., the thermal flux through an overhang is restricted [3]. Constriction of heat to a relatively small area leads to severe thermal gradients within the overhang features which ultimately manifests in distorted builds (termed swelling by Sames *et al.* [5]). If unchecked, distortion will lead to the build making contact with the recoater mechanism. This contact may damage the recoater/roller and the part; jam the recoater; or even peel the part off the build platen.

Second, the impeded heat flux in the overhang may lead to overheating which affects the surface quality and microstructure of the downward facing overhang sections [7]. A practical example of this effect in LPBF of a 316L stainless steel knee implant having an overhang section is evident in Figure 1 (right).

Third, Creaghs *et al.* observed during scanning of the overhang the aspect ratio (length to width) of the meltpool increases [8]. As a consequence, the authors posit, the meltpool becomes unstable due to onset of a phenomena called Plateau-Rayleigh effect and splits into discrete chunks. This disjointed nature of the meltpool is believed to be at the root of the poor surface finish and porosity observed in overhang sections [3]. These effects for building parts with unsupported overhangs was theoretically confirmed by King *et al.* [17]

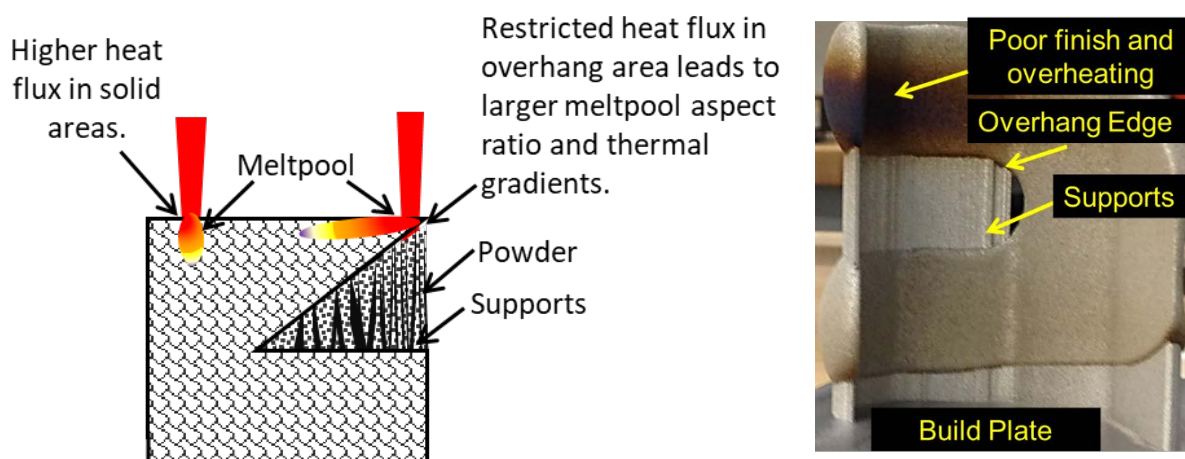


*Figure 1: (left) Illustration of restricted heat flux in the overhang features. (right) Stainless steel 316L knee implant built on a production LPBF machine showing significant overheating and poor surface finish in overhang areas.*

## 2 Proposed Methodology

Application of graph theoretic approaches for signal processing is a nascent domain with recent notable review articles by Hammond *et al.* [13], Sandryhaila *et al.* [12], and Shuman *et al.* [14, 15]. Graph theoretic shift operators and signal transforms are in their infancy [12-15, 18, 19]. Niyogi *et al.* [9-11] in a series of seminal articles proposed embedding high dimensional data as an undirected graph, and subsequently projecting the data into the Eigenvector space of the graph Laplacian[9-11]. A conference on signal processing on graphs, with implications to Big Data was recently organized [20].

- The convention is to denote matrices and vectors with bold typesets. Suppose we gather a sequence of sensor data,  $\mathcal{X}$  (time series or images) from a process. Further, consider that the process manifests in  $n$  different known process conditions or build states labelled as  $s_1, s_2, s_i \dots s_n$ . In LPBF these states could refer to different printing conditions, such as non-overhang, overhang, thin sections, etc. This allows us to apportion the sensor data  $\mathcal{X}$  associated with each state  $s_i$  with the symbol  $\mathbf{x}_i$ . The aim is to identify the system state  $s_i$  from which an unlabeled signal  $y$  is observed; i.e., if we observe a signal  $y$ , we want to find the process state  $i$  to which it belongs.

$$\mathbf{x}_i = \begin{bmatrix} a_1^1 & a_1^2 & \dots & a_1^d \\ a_t^1 & \ddots & & a_t^d \\ \vdots & & & \vdots \\ a_m^1 & \dots & & a_m^d \end{bmatrix}$$

The approach involves three phases; these are described herewith.

Step 1: Transform the signals  $\mathbf{x}_i$  corresponding to each pre-labeled state  $s_i$  into an undirected, weighted network graph  $G_i(V, E, W)$ . Where,  $V$  and  $E$  are the vertices and edges of the graph and  $W$  is the weight between the edges.

Step 2: The spectral graph Laplacian matrix  $\mathcal{L}_i$  is computed from the graph  $G_i$ . The first non-zero  $n$  graph Laplacian Eigenvectors  $\mathbf{v}_i$  are used as an orthogonal basis set corresponding to the process state  $s_i$ .

Step 3: Each  $\mathbf{x}_i$  is decomposed by taking an inner product  $\mathbf{x}_i^T \cdot \mathbf{v}_i$  akin to a Fourier transform into a set of coefficients  $\mathbf{c}_i$  called graph Fourier coefficients.

- The graph Fourier coefficients is written in block matrix form as  $\mathbb{C} = \begin{bmatrix} [\mathbf{c}_1^T] & [\mathbf{c}_2^T] & \dots & [\mathbf{c}_i^T] & \dots & [\mathbf{c}_n^T] \end{bmatrix}$  corresponding to different states  $s_1, s_2, s_i \dots s_n$ . The matrix  $\mathbb{C}$  is called the *dictionary*.

Step 4: Given an unlabeled signal  $y$ , an inner product  $\mathbf{p}_i = y^T \cdot \mathbf{v}_i$  is taken with each of the  $n$  basis vector sets one at a time; where  $n$  are the different states. The matrices  $\mathbf{p}_i^T$  are called the candidate coefficients. Each  $\mathbf{p}_i^T$  is compared with the corresponding  $\mathbf{c}_i^T$  in the dictionary  $\mathbb{C}$  in terms of the

squared error  $e_i$ . The comparison resulting in the least error is the designated Application to Experimental Data from the Laser Powder Bed Fusion Process

## 2.1 Experimental Details and Data Acquisition System

Experiments were conducted on a commercial LPBF machine (EOS M270) at NIST. The machine was integrated with three types of sensors, namely, a SWIR lens thermal camera (1350 – 1600 nm), high-speed video camera (4000 frames per second), and a photodetector. The SWIR thermal camera and photodetector capture the thermal aspects of the meltpool, whereas the high-speed video camera captures its shape and surrounding spatter pattern.

Data was acquired at a sampling rate of 1 MHz. Figure 2 shows the schematic implementation of the setup. The detailed explanation of the setup is available in [21, 22]. The test artifact, which is made from Nickel alloy IN625 (58% Ni, 23% Cr), has a steep overhang of  $40.5^\circ$ . In this work, the sensor information was not captured continuously during the duration of the build, but only for three layers, at 6.06 mm, 7.90 mm, and 9.70 mm. The overhang is also sintered in these layers, rather than the solid portion alone. The process parameters are shown in Table 1. The overarching aim is to distinguish the sensor patterns that emerge during printing of overhang (2 hatches from the edge) and non-overhang features of the part shown in Figure 3.

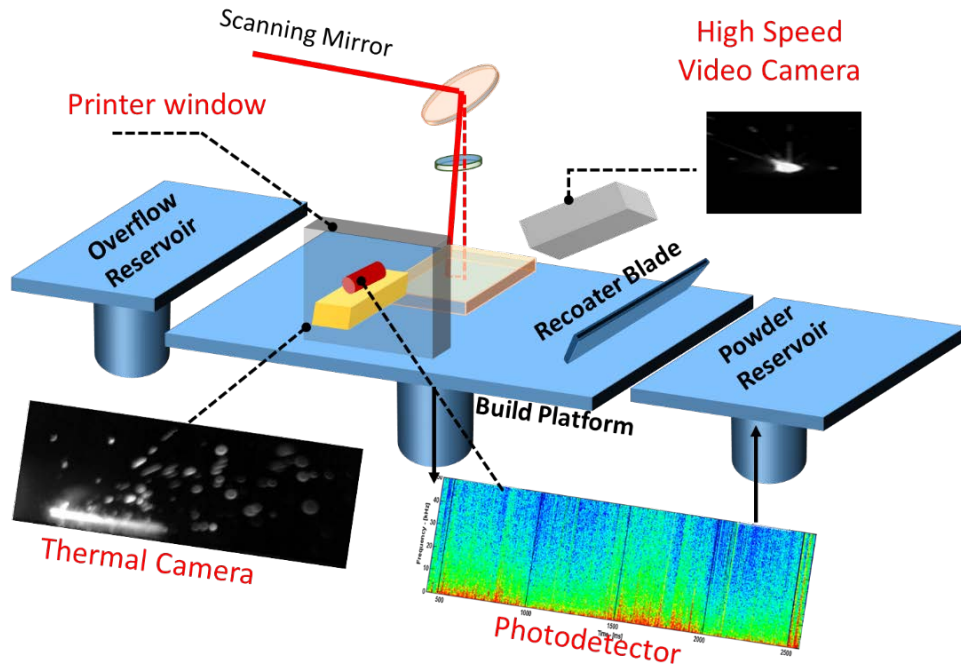


Figure 2: Schematic layout of sensors installed on the LPBF 3D printer.

The part is sintered per the stripe pattern shown in Figure 3(c and d); hence the laser sinters along the overhang four times (called stripes) for each layer past 4 mm build height. The challenge is that the length of time in scanning the overhang portion progressively increases with the build height; therefore, the temperature trends recorded during printing the overhang will progressively increase with the build height. In other words, the process exhibits a nonstationary trend, which limits the use of parametric statistical approaches, such as control charts, which rely on fixed distribution characteristics.

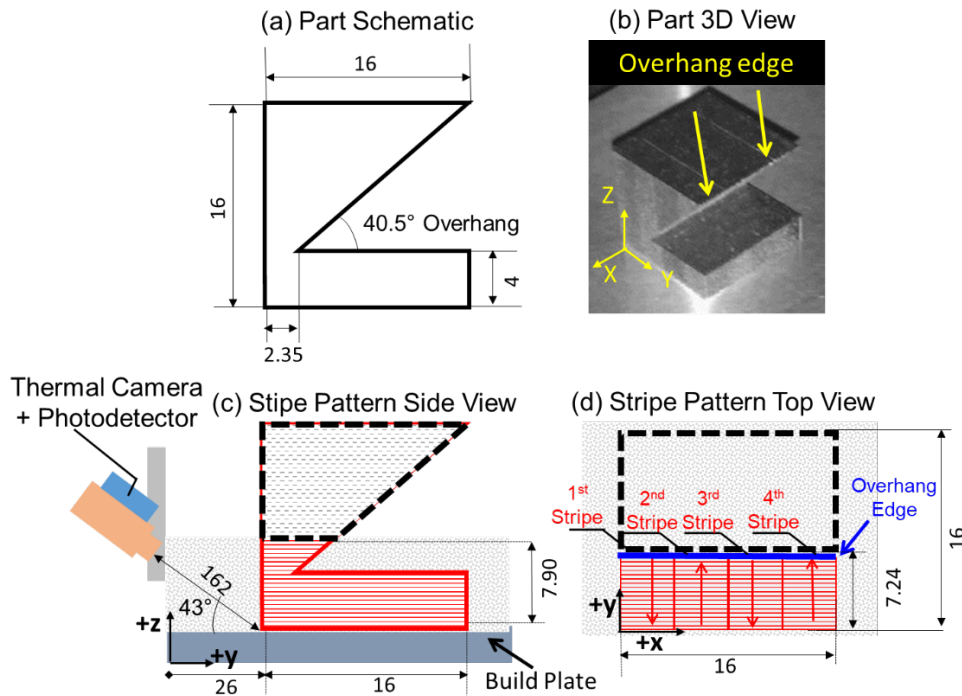


Figure 3: (a) The part schematic (all dimensions in mm, drawings are not to scale) measuring 16 mm on all sides with 40° overhang, (b) as-built without supports, (c and d) Side-view and top views of the stripe pattern at the build height of 7.9 mm in the context of the thermal camera position

Table 1: Printing parameters used for fabrication of overhanging structure

Print Parameter	Value
Hatch distance	0.1 mm
Stripe width	4 mm
Stripe overlap	0.1 mm
Layer thickness	20 μm
Scan speed	800 mm/s
Laser power	195 W (infill) 100 W (pre-contour) 120W (post-contour)

## 2.2 Statistical Analysis of the Data

### (a) Image Processing

The aim of this section is to apply image processing and statistical signal analysis approaches to differentiate between OH and NOH printing conditions. The intent is to isolate the sensor signatures including melt pool and spatter pattern during different build conditions - overhang (OH) and non-overhang (NOH) edge - from the thermal and high-speed video camera. A series of steps involving popular image processing procedures is implemented.

Step 1: Each image frame was converted to a binary black and white image; the threshold value was selected heuristically and remains fixed. The image obtained after binarization is represented as  $I_b$

Step 2: The aim is to isolate specific aspects of the meltpool, such as its size and spatter pattern. However, these are difficult to obtain without loss of information from the binarized image  $I_b$ . As a result, we create a binary mask  $I_m$  specific to the meltpool shape and the spatter pattern by following the procedure summarized herewith:

- Detecting the connected pixel components in the binary image  $I_b$ ; this is done using the matlab routine (*imbinarize*). This routine determines whether, and to what degree a given pixel is connected to its nearest neighbors. The rationale is that a pixel in the meltpool region is well-connected to its neighbors (because the meltpool presents a larger contiguous area), compared to a pixel from the spatter pattern.
- Isolating the component (filtering away the components which have low connectivity). This leaves the largest area, i.e., the meltpool shape, subsequently, and subtracting the meltpool from  $I_b$  results in the binary image with the spatter pattern. This image with the binary meltpool and spatter pattern is called the mask  $I_m$ .
- A Hadamard product (element-wise multiplication)  $I_m \cdot I_o = I_f$  yields images with the specific meltpool and spatter aspects retained. The resulting isolated meltpool and spatter pattern  $I_f$  for both the overhang and non-overhang conditions are shown in Figure 5.

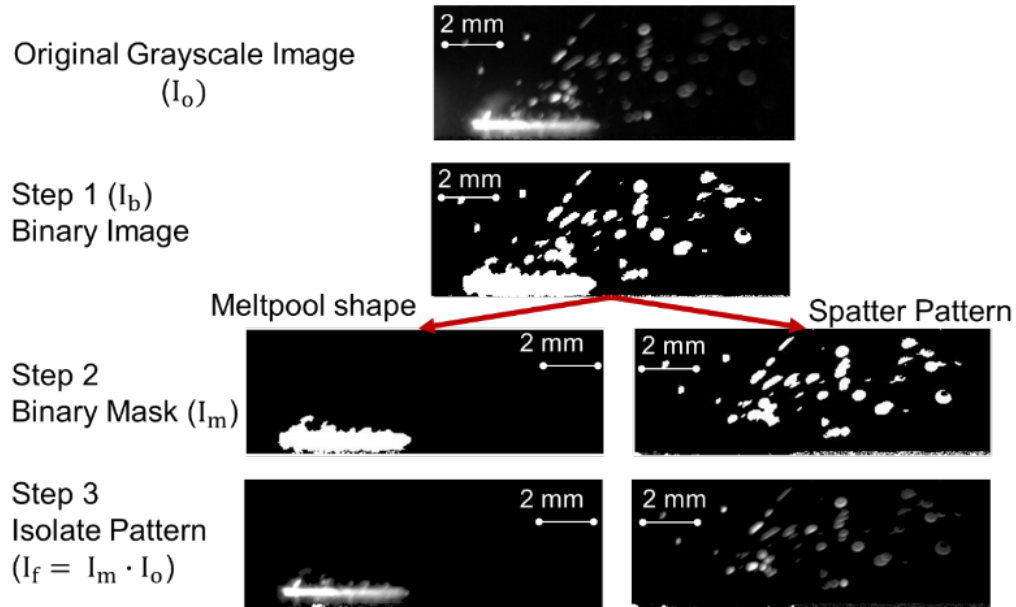


Figure 4: Isolating the thermal signatures (melt pool and spatter pattern) using the sequence of image processing steps described.

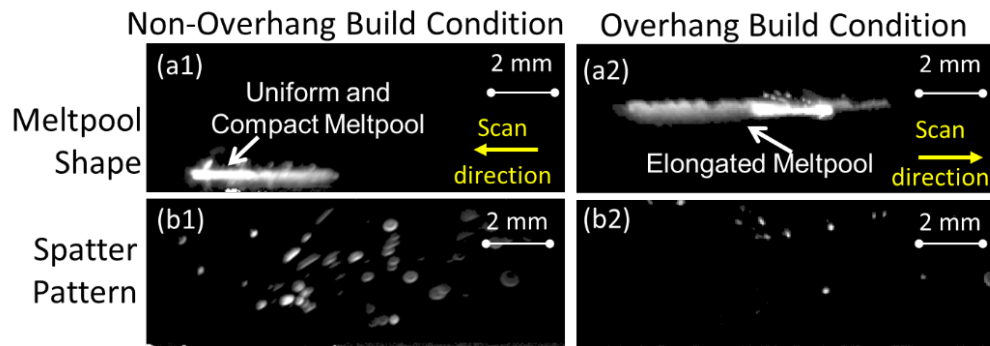


Figure 5: The isolated thermal frame ( $I_f$ ) for (a1 and a2) meltpool shape and (b1 and b2) spatter pattern for the overhang and non-overhang build conditions, respectively. Note the elongated shape of the meltpool in (a2).

Two statistical features are defined on the isolated pattern  $I_f$ . The first is the sum of intensities for each column of  $I_f$ . This feature is called column intensity ( $J_\Sigma$ ). The second feature is based on plotting a histogram of pixel intensities in the isolated frame ( $I_f$ ). This feature is called the histogram count ( $J$ ). The procedure is shown schematically in Figure 6 (a) and (b) for  $J_\Sigma$  and  $J$  respectively.

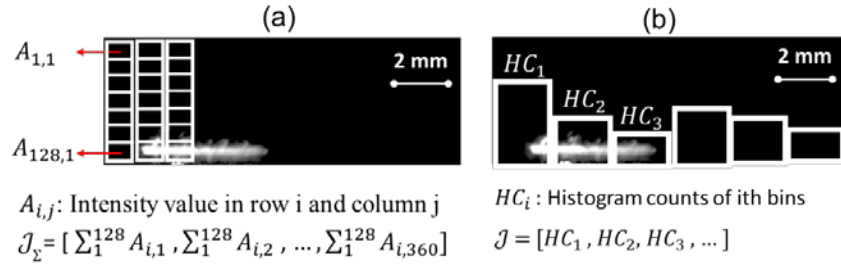


Figure 6: Two statistical features used for analysis of meltpool shape (a) column intensity (b) histogram counts

Shown in Figure 7 are the empirical cumulative distribution functions (ecdf) of the meltpool and spatter histogram counts ( $J$ ) and column intensities ( $J_{\Sigma}$ ) for three overhang (OH) and non-overhang (NOH) build conditions.

- Figure 7 (a1) and (a2) concern the meltpool histogram counts ( $J$ ) and column intensities ( $J_{\Sigma}$ ) respectively; the corresponding distributions for the spatter pattern are shown in Figure 7 (c) and (d). The following inference can be drawn from Figure 7.
- The ecdf of meltpool histogram counts ( $J$ ) in Figure 7 (a1) cannot be visually distinguished. The ecdf distribution of  $J$  for spatter is shown in Figure 7 (b1), and is able to discriminate between OH and NOH conditions.
- Well-known statistical distributions, such as normal, exponential, Weibull, extreme value, Beta, etc., were unable to explain (or fit) the ecdf for  $J$  nor  $J_{\Sigma}$ .

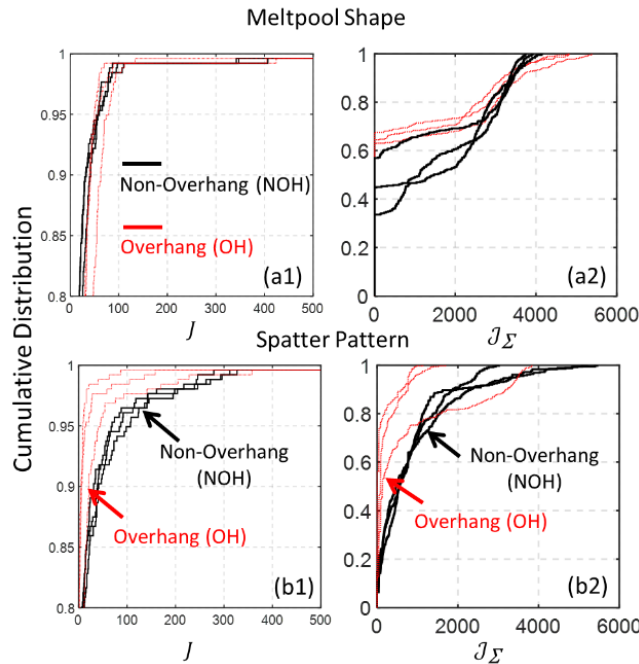


Figure 7: Empirical cumulative distribution functions of thermal camera (a1 and a2) meltpool shape and (b1) and (b2) spatter pattern based on the histogram counts ( $J$ ) and column intensities ( $J_{\Sigma}$ ).

For instance, the probability plot for fitting the versatile Weibull statistical distribution on the spatter histogram counts ( $J$ ) is shown in Figure 8. In a good distribution the observations (histogram counts in our analysis) will fall within the confidence intervals. As observed from the probability plot, both tails of the ecdf deviates from the Weibull distribution; results for other distributions are worse. Hence, statistical analysis based on parametric distributions are found to be inadequate. This analyses were repeated with images obtained from the high-speed camera; the difference between the OH and NOH states was undistinguishable.

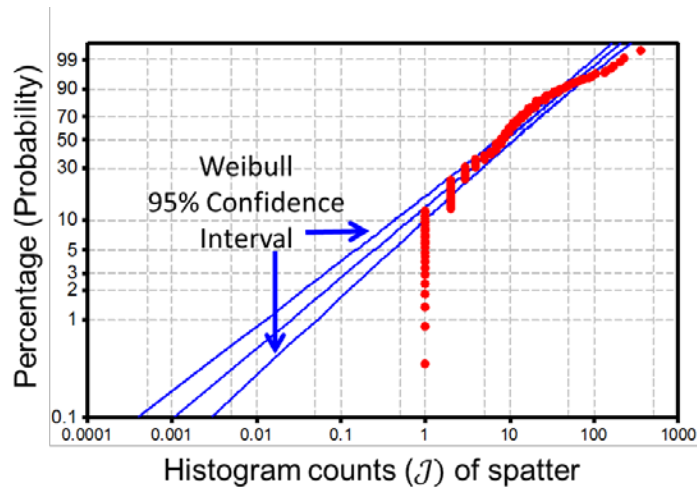


Figure 8: Probability plot for fitting Weibull distribution to thermal camera histogram counts for spatter pattern

(b) Time-Frequency Analysis of the Photodetector Signal.

The spectrogram is a widely used tool to capture the time-frequency and amplitude aspects of a signal simultaneously [23]. To obtain the spectrogram for the photodetector data, it is necessary to align the signal with the thermal camera frame (as the position information is not available). A spectrogram is essentially a short time Fourier transform (STFT) taken over several windows of a signal. In other words, the thermal camera data is used as the so-called ground truth for distinguishing between the OH and NOH build conditions. As mentioned before, one frame of thermal camera translates to 555 data points (~ 555 microseconds) for the photodetector. As in the thermal image analysis in Sec. 2.2(a), the spectrogram analysis for two representative OH and NOH signals are shown in Figure 9.

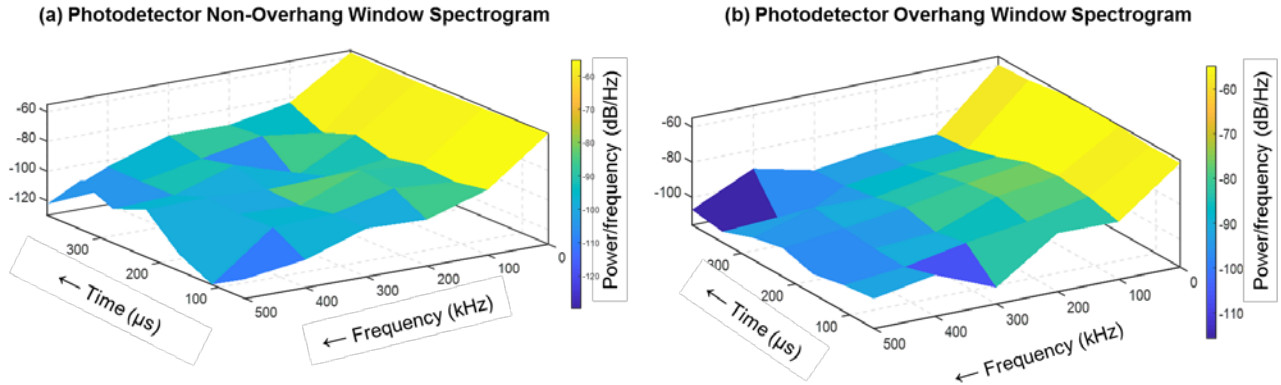


Figure 9: Spectrogram of the photodetector signal in (a) overhang and (b) non-overhang printing conditions for one layer. Note that there is no discernable difference in the shape and magnitude of the frequency spectrum.

Although a visual comparison between the overhang (OH) and non-overhang (NOH) spectrogram issues no significant difference, the patterns were statistically analyzed. Figure 10 shows the aggregate power spectral density (PSD) scatterplot in three different frequency bands of the photodetector signal, namely, 0-100 KHz, 200-300 KHz and 400-500 KHz for the overhang (OH) and non-overhang (NOH) build condition.

A 2-sample t-test was performed to assess the hypothesis that there was no significant difference in mean PSD between the OH and NOH build conditions at each of the frequency bands. This hypothesis was rejected for the 400-500 KHz frequency band at the 95% confidence level; i.e., there is indeed a statistical difference in the PSD for the OH and NOH cases. Nonetheless, a statistical difference does not guarantee high classification fidelity, i.e., concluding the state of the build (OH vs. NOH) given a PSD is difficult due to the high variability as evidenced by the scatter plot in Figure 10.

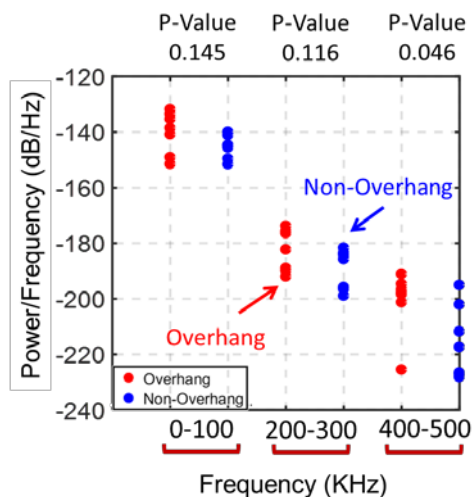


Figure 10: Scatter plot of power spectral densities at three different frequencies (0 – 100 KHz, 200-300 KHz and 400-500 KHz) with the p-value related to the 2 sample t-test.

### 2.3 Spectral Graph Theoretic Analysis

The aim of this section is to apply the spectral graph approach described in Sec. 2 to discriminate between the overhang and non-overhang build conditions. The approach is compared against seven other popular machine learning approaches. For brevity, the parameter settings are encapsulated in the Appendix. Table 2 represents the performance of the spectral analysis algorithm for all three types of sensor signals in terms of F-score value.

Table 2: Results from applying the proposed approach to each of the three types of sensor signals.

(a) The percentage F-score results for detecting the two printing conditions in thermal camera, visible camera and photodetector, the numbers in parenthesis represents the standard deviation from a five-fold replication (data from three layers).

Sensor	Data Dimension	Proposed Approach	LD	KNN	Tree	SVM	Boosted Trees	NN	QDA
Thermal Camera	2D (128×360)	0.95 (0.01)	0.36 (0.02)	0.5 (0.02)	0.38 (0.03)	0.42 (0.03)	0.43 (0.03)	0.40 (0.02)	0.6 (0.02)
Visible Camera	2D (256×256)	0.83 (0.02)	0.58 (0.02)	0.57 (0.03)	0.61 (0.01)	0.63 (0.02)	0.62 (0.01)	0.54 (0.00)	0.5 (0.01)
Photodetector	1D (555 × 1)	0.79 (0.01)	0.59 (0.02)	0.6 (0.02)	0.62 (0.01)	0.61 (0.01)	0.61 (0.02)	0.6 (0.01)	0.5 (0.01)

(b) The confusion matrix for detecting the two printing conditions (overhang (OH), and non-overhang (NOH)) from the thermal camera, high-speed camera and photodetector. The data is for 250 randomly chosen sequences from each build condition.

		Predicted Build Condition		
		Overhang (OH)	Non-Overhang (NOH)	
Actual Process Condition	Thermal Camera	OH	250	0
		NOH	24	226
	Visible Camera	OH	250	0
		NOH	83	167
	Photodetector	OH	157	93
		NOH	9	241

### 3 Conclusions and Future Work

This work proposed a spectral graph theoretic approach for monitoring the build status in laser powder bed fusion (LPBF) additive manufacturing (AM) process via a heterogeneous sensing array consisting of a photodetector, SWIR thermal camera, and high-speed video camera. The central idea of the approach is to convert the sensor data into a lower dimensional manifold, specifically, a weighted and undirected network graph. The intuition is that the topology of the graph is a surrogate indicator of the build states. Based on this premise, we tested the hypothesis that by quantifying and learning the signal patterns embedded in the topology of the network graph in terms its Laplacian Eigenvectors, process phenomena indicative of the build status is detected

with higher fidelity compared to conventional machine learning approaches. The specific conclusion is as follows.

The proposed graph theoretic approach was applied to the sensor data with the intent to distinguish between the OH and NOH build states, the F-score obtained in the region of 80 to 95%, contingent on the type of sensors:

- F-score ~ 95% from the SWIR thermal camera
  - F-score ~ 83% for the high-speed video camera
  - F-score ~ 79% for the photodetector sensor.
- What other different types and more relevant microstructure-level defects, such as powder contamination, poor fusion, porosity delamination, etc., may be detected?
  - What is the link between specific defects and sensor signal patterns? In other words, is there a one-to-one link between a type of defect and its severity, and the sensor signature it manifests?
  - What is the detection lag; does the detection accuracy improve with sensor redundancy?

### **Acknowledgements**

The authors acknowledge the contribution of Dr. Brandon Lane and Dr. Jarred Heigel of the National Institutes of Standards and Technology (NIST), United States Department of Commerce; the data for this work was generated at NIST. Dr. Lane and Dr. Heigel do not appear on the list of authors of the article in the conference proceedings pending review of its scientific merits and subsequent approval by NIST's editorial review board per established policy.

## References

- [1] I. Gibson, D. W. Rosen, and B. Stucker, *Additive manufacturing technologies: rapid prototyping to direct digital manufacturing*. Springer, 2010.
- [2] J. z. Jacobsmuhlen, S. Kleszczynski, D. Schneider, and G. Witt, "High resolution imaging for inspection of Laser Beam Melting systems," in *2013 IEEE International Instrumentation and Measurement Technology Conference*, 2013, pp. 707-712: IEEE.
- [3] S. Kleszczynski, J. Zur Jacobsmühlen, J. Sehr, and G. Witt, "Error detection in laser beam melting systems by high resolution imaging," in *Proceedings of the Twenty Third Annual International Solid Freeform Fabrication Symposium*, 2012.
- [4] B. Foster, E. Reutzel, A. Nassar, B. Hall, S. Brown, and C. Dickman, "Optical, layerwise monitoring of powder bed fusion," in *Solid Free. Fabr. Symp. Proc*, 2015, pp. 295-307.
- [5] W. J. Sames, F. List, S. Pannala, R. R. Dehoff, and S. S. Babu, "The metallurgy and processing science of metal additive manufacturing," *International Materials Reviews*, vol. 61, no. 5, pp. 315-360, 2016.
- [6] G. Repossini, V. Laguzza, M. Grasso, and B. M. Colosimo, "On the use of spatter signature for in-situ Monitoring of Laser Power Bed Fusion," *Additive Manufacturing*, vol. 16, pp. 35-48, 2017.
- [7] T. Craeghs, S. Clijsters, J. P. Kruth, F. Bechmann, and M. C. Ebert, "Detection of Process Failures in Layerwise Laser Melting with Optical Process Monitoring," *Physics Procedia*, vol. 39, pp. 753-759, 2012.
- [8] T. Craeghs, S. Clijsters, E. Yasa, F. Bechmann, S. Berumen, and J.-P. Kruth, "Determination of geometrical factors in Layerwise Laser Melting using optical process monitoring," *Optics and Lasers in Engineering*, vol. 49, no. 12, pp. 1440-1446, 2011.
- [9] M. Belkin and P. Niyogi, "Laplacian eigenmaps for dimensionality reduction and data representation," *Neural computation*, vol. 15, no. 6, pp. 1373-1396, 2003.
- [10] M. Belkin and P. Niyogi, "Semi-supervised learning on Riemannian manifolds," *Machine learning*, vol. 56, no. 1-3, pp. 209-239, 2004.
- [11] P. Niyogi and X. He, "Locality preserving projections," in *Neural information processing systems*, 2004, vol. 16, p. 153: MIT.
- [12] A. Sandryhaila and J. M. Moura, "Discrete signal processing on graphs," *IEEE transactions on signal processing*, vol. 61, pp. 1644-1656, 2013.
- [13] D. K. Hammond, P. Vandergheynst, and R. Gribonval, "Wavelets on graphs via spectral graph theory," *Applied and Computational Harmonic Analysis*, vol. 30, no. 2, pp. 129-150, 2011.

- [14] D. I. Shuman, S. K. Narang, P. Frossard, A. Ortega, and P. Vandergheynst, "The emerging field of signal processing on graphs: Extending high-dimensional data analysis to networks and other irregular domains," *IEEE Signal Processing Magazine*, vol. 30, no. 3, pp. 83-98, 2013.
- [15] D. I. Shuman, B. Ricaud, and P. Vandergheynst, "A windowed graph Fourier transform," in *2012 IEEE Statistical Signal Processing Workshop (SSP)*, 2012, pp. 133-136: Ieee.
- [16] O. DeJesús and M. T. Hagan, "Backpropagation through time for a general class of recurrent network," in *11th International Joint Conference on Neural Networks*, Washington, D.C., 2001, pp. 2638-2642, Washington, D.C.
- [17] W. King, A. Anderson, R. Ferencz, N. Hodge, C. Kamath, and S. Khairallah, "Overview of modelling and simulation of metal powder-bed fusion process at Lawrence Livermore National Laboratory," *Materials Science and Technology*, 2014.
- [18] J. D. Lee and M. Maggioni, "Multiscale analysis of time series of graphs," in *Proceedings of The 9th International Conference on Sampling Theory and Applications*, Singapore, 2011.
- [19] X. Zhu and M. Rabbat, "Graph spectral compressed sensing for sensor networks," in *IEEE International Conference on Acoustics, Speech and Signal Processing (ICASSP)*, Kyoto, Japan, 2012, pp. 2865-2868: IEEE.
- [20] p. f. G. S. P. Workshop, in *Graph Signal Processing Workshop*, Philadelphia, PA, 2016.
- [21] B. Lane *et al.*, "Thermographic measurements of the commercial laser powder bed fusion process at NIST," *Rapid prototyping journal*, vol. 22, no. 5, pp. 778-787, 2016.
- [22] B. Lane, E. Whinton, and S. Moylan, "Multiple sensor detection of process phenomena in laser powder bed fusion," in *SPIE Commercial+ Scientific Sensing and Imaging*, 2016, pp. 986104-986104-9: International Society for Optics and Photonics.
- [23] S. Qian and D. Chen, *Joint time-frequency analysis: methods and applications*. Prentice-Hall, Inc., 1996.